The Lyman Continuum Escape Survey: Connecting Time-dependent [O III] and [O II] Line Emission with Lyman Continuum Escape Fraction in Simulations of Galaxy Formation

Kirk S. S. Barrow[1] , Brant E. Robertson[2] , Richard S. Ellis[3] , Kimihiko Nakajima[4] , Aayush Saxena[3] , Daniel P. Stark[5], and Mengtao Tang[3,5]

[1] Kavli Institute for Particle Astrophysics and Cosmology, Stanford University, 452 Lomita Mall, Stanford, CA 94305-4085, USA; kssbarrow@gmail.com
[2] Department of Astronomy & Astrophysics, University of California, Santa Cruz, 1156 High Street, Santa Cruz, CA 95064, USA
[3] Department of Physics and Astronomy, University College London, Gower Street, London WC1E 6BT, UK
[4] National Astronomical Observatory of Japan, 2-21-1 Osawa, Mitaka, Tokyo 181-8588, Japan
[5] Steward Observatory, University of Arizona, 933 N. Cherry Avenue, Tucson, AZ 85721, USA
Received 2020 September 15; revised 2020 September 30; accepted 2020 October 1; published 2020 October 20

Abstract

Escaping Lyman continuum photons from galaxies likely reionized the intergalactic medium at redshifts $z \gtrsim 6$. However, the Lyman continuum is not directly observable at these redshifts and secondary indicators of Lyman continuum escape must be used to estimate the budget of ionizing photons. Observationally, at redshifts $z \sim 2\text{–}3$ where the Lyman continuum is observationally accessible, surveys have established that many objects that show appreciable Lyman continuum escape fractions $f_{\rm esc}$ also show enhanced [O III]/[O II] (O_{32}) emission line ratios. Here, we use radiative transfer analyses of cosmological zoom-in simulations of galaxy formation to study the physical connection between $f_{\rm esc}$ and O_{32}. Like the observations, we find that the largest $f_{\rm esc}$ values occur at elevated $O_{32} \sim 3\text{–}10$ and that the combination of high $f_{\rm esc}$ and low O_{32} is extremely rare. While high $f_{\rm esc}$ and O_{32} often are observable concurrently, the timescales of the physical origin for the processes are very different. Large O_{32} values fluctuate on short (~ 1 Myr) timescales during the Wolf–Rayet-powered phase after the formation of star clusters, while channels of low absorption are established over tens of megayears by collections of supernovae. We find that while there is no direct causal relation between $f_{\rm esc}$ and O_{32}, high $f_{\rm esc}$ most often occurs after continuous input from star formation-related feedback events that have corresponding excursions to large O_{32} emission. These calculations are in agreement with interpretations of observations that large $f_{\rm esc}$ tends to occur when O_{32} is large, but large O_{32} does not necessarily imply efficient Lyman continuum escape.

Unified Astronomy Thesaurus concepts: Emission nebulae (461); Radiative transfer simulations (1967); Galaxy formation (595); Interstellar line emission (844); Star forming regions (1565); High-redshift galaxies (734); High time resolution astrophysics (740)

1. Introduction

The process of cosmic reionization represents a major challenge for understanding the large-scale evolution of the intergalactic medium (IGM). Reionization completed during the first billion years of cosmic history, as evidenced by the prominent Gunn & Peterson (1965) absorption troughs from neutral hydrogen observed in the spectra of quasars at redshifts $z > 6$ (Fan et al. 2001, 2006; Bañados et al. 2018). Given the rapid decline in the abundance of bright quasars over the same epoch, star-forming galaxies at high redshift likely produced the Lyman continuum photons required to reionize the IGM (Bouwens et al. 2015; Robertson et al. 2015; Finkelstein et al. 2019). The opacity of the mostly ionized IGM at late times remains high enough to prevent the direct detection of Lyman continuum (LyC) photons far beyond redshift $z \sim 3$ (Madau 1995; Steidel et al. 2001; Inoue et al. 2014). During the reionization epoch, probes of the potential LyC production and escape must rely on secondary observational indicators, such as nebular emission lines from galaxies, that the forthcoming James Webb Space Telescope (JWST) will examine in detail. Motivated by the need to understand the physics behind secondary indicators of LyC escape, this Letter presents radiative transfer calculations in high-resolution hydrodynamical simulations of galaxy formation to study the connection between LyC escape fraction $f_{\rm esc}$ and rest-frame

optical emission lines powered by ionizing radiation from massive stars.

Given the importance of understanding how galaxies might reionize the IGM, the search for evidence of escaping LyC photons has been wide-ranging. Searches of nearby galaxies have detected LyC emission in some unusually compact or star-bursting galaxies (Borthakur et al. 2014; Izotov et al. 2016a, 2016b; Leitherer et al. 2016). Blue-sensitive spectrographs have provided direct spectroscopic evidence for LyC emission (Steidel et al. 2001; Shapley et al. 2006; Steidel et al. 2018), as has ground-based continuum imaging (Iwata et al. 2009; Vanzella et al. 2010; Nestor et al. 2011, 2013; Mostardi et al. 2013; Grazian et al. 2016; Meštrić et al. 2020). Owing to the need for high-resolution imaging in identifying potential foreground contamination (Vanzella et al. 2012; Mostardi et al. 2015), many recent searches for LyC have focused on redshifts $z \sim 2\text{–}3$, where ultraviolet (UV) filters on Hubble Space Telescope (HST) probe blueward of 912 Å in the galaxy rest frame. These efforts include our LymAn Continuum Escape Survey (LACES, HST GO-14747; Fletcher et al. 2019) that has to-date focused on observational connections between LyC escape and the ionizing photon production evidenced by nebular line emission in galaxies (Nakajima et al. 2020). These direct searches have been complemented by studies of the association of LyC production with ultraviolet or optical nebular lines (Tang et al. 2019; Du et al. 2020), the

correspondence between Lyα and the ([O III]λ5007 + [O III] λ4959)/[O II]λ3727 line ratio (O₃₂) (Izotov et al. 2020), and the link between LyC escape, Hβ emission, and the rest-frame UV spectral slope (Yamanaka et al. 2020).

Relating LyC and optical emission lines at high redshift currently requires infrared spectrographs on ground-based large telescopes that can access redshifted rest-frame ultraviolet and optical lines (Nakajima et al. 2016, 2018). Studies of the LyC-line emission connection are motivated in part by the analyses by Jaskot & Oey (2013) and Nakajima & Ouchi (2014), who suggested that the structure of photoionization regions within a galaxy may induce a connection between $f_{\rm esc}$ and O₃₂. Many galaxies with LyC detections at redshifts $z \sim 2$–3 do indeed show elevated O₃₂ and combined ([O III]λ5007 + [O III]λ4959 + [O II]λ3727)/Hβ λ4861 measure known as R_{23}, but not all strong line emitters display escaping LyC (Naidu et al. 2018; Bassett et al. 2019; Jaskot et al. 2019) and active galactic nuclei may contribute to a portion that do (Smith et al. 2018, 2020).

In this Letter, radiative transfer calculations are applied to simulations of galaxy formation to study how LyC escape and optical line emissions are physically connected. The radiative transfer of LyC photons from galaxies has been examined in cosmological simulations of galaxy formation (e.g., Ma et al. 2016; Trebitsch et al. 2017), where feedback from star formation was shown to play an important role in enabling hydrogen ionizing photons to escape into the IGM. Previous studies are extended by additionally examining time-dependent [O III] and [O II] line emission, and their relation to the ionizing photon production of newly formed stars (see also Katz et al. 2020). We show for the first time that galaxy population statistics of $f_{\rm esc}$ and O₃₂ may be explained by these time-dependent processes.

2. Methods

2.1. Cosmological Simulation

Results are based on a radiation-hydrodynamic adaptive mesh refinement ENZO (Bryan et al. 2014) simulation evolved from initial conditions produced as part of the AGORA collaboration (Kim et al. 2014). The simulation is run with cosmological parameters $\Omega_M = 0.3065$, $\Omega_\Lambda = 0.6935$, $\Omega_b = 0.0483$, $h = 0.679$, $\sigma_8 = 0.8344$, and $n = 0.9681$, which are taken from the most recent release of the Planck Collaboration et al. (2020). Within a 5 Mpc³ box with a root grid size of 128³, a smaller 625 × 703.125 × 1093.75 kpc³ subgrid encompassing the Lagrangian volume of a 10¹⁰ M⊙ halo (at $z = 0$) is refined by a factor of 2⁴ to create an effective grid size resolution of (2048)³ with a dark matter particle mass of 1043 M⊙. Inside this smaller *zoom-in* region, grids are allowed to further refine adaptively to up to a factor of 2¹⁴ more than the root grid dimensions as successive density thresholds are exceeded. At $z = 4$ this corresponds to a minimum proper cell width of ∼0.70 pc, but typical values are between 11 and 180 proper parsecs within the virial radius of the largest halo at that redshift. The simulation includes nine-species (H I, H II, He I, He II, He III, e⁻, H₂, H₂⁺, H⁻) radiatively driven, nonequilibrium chemistry, radiating star particles, and supernovae feedback (Wise et al. 2012) with the same parameters and thresholds described in Barrow (2019).

To facilitate analysis of the time-dependence of emission line trends, the state of the simulation is saved every 368,000 yr starting at $z = 6$ until $z = 3$, which corresponds to about 3400

outputs. In the simulation, a major merger ($M_\star = 4.69 \times 10^7 M_\odot$; $M_\star = 3.21 \times 10^7 M_\odot$) begins at $z \sim 4.17$ and concludes at $z \sim 3.5$. Therefore, two significant halos of roughly similar mass are available for study from $z = 6$ until their merger. The larger halo at the time of merger and their resulting combined halo is henceforth referred to as Halo 0 and the smaller member of the merger will be referred to as Halo 1. At $z = 6$, Halo 1 has almost twice the stellar mass as Halo 0 ($M_\star = 1.63 \times 10^7 M_\odot$ versus $M_\star = 8.33 \times 10^6 M_\odot$), but subsequently exhibits a slower star formation rate. At $z = 3.5$, the stellar mass and total mass of Halo 0 grows to $2.01 \times 10^8 M_\odot$ and $1.23 \times 10^9 M_\odot$ respectively.

2.2. Emission Line Model

Emission lines are calculated in roughly the same manner as in Barrow (2019), with some small improvements and additions. To summarize, a halo merger tree is produced by performing an iterative r_{200} overdensity-finding algorithm tuned to return a consistent halo position and radius between timesteps as well as track Halo 1 through its merger. Then, using Flexible Stellar Population Synthesis (FSPS; Conroy & Gunn 2010), 8000-wavelength spectra are attached to each star particle based on its age, metallicity isochrone, and mass at each timestep.

From these spectra, a mean galactic spectrum is estimated and combined with the mean metallicity and density of the halo to produce wavelength-dependent absorption cross sections for the gas at 200 temperatures between $10^{2.5}$ and 10^7 K using the CLOUDY photoionization solver (Ferland et al. 2017). These look up tables are separately generated for each halo and timestep and are attached to the combined mass of absorbers from simulation cells (H I, He I, He II, H₂, H₂⁺, H⁻, and metals) as well as the cell temperature along rays to estimate the spectra and flux distribution within the halo. In a test, analytic models for the ionization cross sections of H I, He I, and He II attached to the corresponding densities from the simulation for comparison. Therein, absorption along rays were roughly equivalent (within 5%) to the CLOUDY-generated model at low to moderately high ionization fractions and a bit less absorptive at very high ionization fractions as the importance of H I diminishes and other processes and species dominate the cross section. Because the cross section is only attached to the strong absorbers in the simulation and the cross sections are generated in the presence of the current galactic spectra, much of the nonequilibrium state of the simulation is preserved with this method, while additionally accounting for absorption phenomena that are not explicitly treated in the simulation.

Armed with a model for the attenuated spectra and flux at every point in a halo, a second round of CLOUDY calculations is used with a geometry prescription that matches the volume distribution of the flux within each cell to carefully account for the presence of multiple stellar sources as discussed in Barrow (2019), and the resulting emission line luminosities are saved and reported. The prior study used a fixed photon path length to cell width ratio at this stage, whereas the cell photon path length used for the purposes of this calculation is estimated to be the luminosity-weighted mean path length from the stars through the cell to a point with low (1st percentile) flux within the cell. Accordingly, the effective path length may be smaller than the smallest dimension of the cell up to the $\sqrt{3}$ times the width of the cell depending on the distribution of stars with respect to the cell as well as their luminosity.

2.3. Escape Fraction and Dust Accounting

This work describes the relationship between O_{32} and the escape fraction of ionizing radiation, f_{esc}, which can be absorbed by both gas and galactic dust. The absorption cross sections used to attenuate stellar light for the emission line model include dust grain extinction, which is implicitly connected to the hydrogen nucleon column density through the use of the mean galactic metallicity in their determination. In this approximation, f_{esc} is calculated as

$$f_{esc} = \sum_{k=1}^{N_{stars}} \frac{\int_{\nu_l}^{\infty} L_{\nu,k} e^{-\tau_\nu} d\nu}{\int_{\nu_l}^{\infty} \sum_{j=1}^{N_{stars}} L_{\nu,j} d\nu}, \qquad (1)$$

where $L_{\nu,k}$ is the spectral luminosity of star k at frequency ν in units of erg s^{-1} Hz^{-1}, ν_l is the frequency of the Lyman limit, and the optical depth, τ_ν, is defined as

$$\tau_\nu = \int_{\vec{r}_{star}}^{\vec{r}_{rvir}} \sigma(T(\vec{r}), \nu) \rho_{tot}(\vec{r}) d\vec{r}, \qquad (2)$$

where $\rho_{tot}(\vec{r})$ is the summed density of strong absorbers at position $\vec{r}$ and $\sigma(T(\vec{r}), \nu)$ is the temperature-dependent mass attenuation coefficient at position $\vec{r}$ as well as frequency ν. Equation (2) is a linear path integral from the position of each star particle, $\vec{r}_{star}$, to a point on the surface of a sphere defined by the virial radius of the halo, $\vec{r}_{rvir}$, along a vector drawn from 1 of 972 Hierarchical Equal Area isoLatitude Pixelations (HEALPIX; Górski et al. 2005) of a sphere. Thus, f_{esc} is a projection of the virial sphere in each HEALPIX direction, simulating parallel rays to an observer from each light source, but not accounting for emission and absorption outside of the virial radius. Depending on the direction, f_{esc} varies wildly owing to the nonhomogeneous nature of optical depths among paths through simulated galaxies. While our calculation of the escape fraction employs ray tracing at the best resolution available to the simulation, there is some evidence that further resolving cloud structures might affect the morphology of H II regions immediately after star formation (e.g., Geen et al. 2015) and further investigations are needed to determine how this might affect galaxy escape fractions.

Because [O III]λ5007 and λ4959 are at longer wavelengths than the [O II]λ3727 doublet and UV/optical dust extinction decreases as a function of wavelength, the presence of dust can increase O_{32} at the virial radius relative to its intrinsic value in H II regions. The boost in the ratio between lines at a wavelength A and a wavelength B due solely to dust extinction can be modeled as $B_{A/B} = e^{\tau_B - \tau_A}$. If one assumes a similar path length from line emitting regions that produce line A and line B to the virial radius, in terms of the dust column mass density, N_{dust} in g cm^{-2}, and the mass attenuation coefficients, σ, the boost is $B_{A/B} \leqslant (e^{N_{dust,max}})^{\sigma_B - \sigma_A}$. Using the relationship between neutral hydrogen nucleon column density, N_H, and dust column mass density described in Draine (2011), the luminosity-weighted maximum value of N_{dust} in either halo during the course of the simulation from sources to the virial radius among any of the HEALPIX directions is

$$N_{dust,max} \leqslant 0.0091 \frac{[O/H]_{max}}{[O/H]_\odot} m_H N_{H,max}$$
$$\leqslant 4.4 \times 10^{-6} \text{ g cm}^{-2}, \qquad (3)$$

where m_H is the mass of hydrogen and assuming a solar abundance of oxygen. Among the Draine (2003) $R_\nu = 3.1$, 4.0, and 5.5 dust models, which span the gamut of dust grain compositions and sizes, the maximum value of $\sigma_{3727\text{Å}} - \sigma_{5007\text{Å}}$ is $\approx$5690 cm^2 g^{-1}. This yields a maximum value of $B_{5007\text{Å}/3727\text{Å}}$ of 1.025, or a 2.5% percent boost. Because this calculation neglects dust scattering, which would further lower the boost by returning a fraction of scattered photons back to the line of sight, and also neglects evidence that lower-metallicity galaxies like the halos in this study have lower dust to N_H ratios (e.g., Rémy-Ruyer et al. 2014; Kahre et al. 2018), the dust correction to the intrinsic O_{32} is likely functionally negligible and certainly less than 2.5%. Therefore, only intrinsic O_{32} values are reported in this study. The same argument applies to R_{23}, since Hβ is also optically thin and of intermediate wavelength between [O II]λ3727 and [O III]λ4959.

Figure 1 visually summarizes the data products from the pipeline during a key point in time where Halo 0 exhibits low O_{32} and high ionizing continuum escape fraction, which is further explored and described in the results section.

2.4. Toy Cluster Model

Since the emission lines derived from the simulation exist within a rapidly evolving cosmological environment, a toy model is also devised to clarify trends that exist within star clusters independently of galaxy dynamics. Using just an FSPS model, CLOUDY, and a Lamers et al. (2005) cluster mass evolution prescription, trends in [O III] and [O II] are computed and plotted in Figure 2 (see the caption for more details).

At the onset of star formation, O_{32} peaks above one since the [O III] emission peaks $\sim$1.5 Myr before the initial peak in [O II] emission. In the range of ($\sim$3.7–5.2 Myr) after the cluster forms, a second, stronger O_{32} peak occurs because the strength of the [O II]λ3727 doublet decays over the first few million years after a star formation event and the harder spectra from the Wolf–Rayet phase of stars in the cluster suddenly converts the reservoir of [O II] to [O III].

Since oxygen coincidentally has almost the same ionization energy as hydrogen, [O II]λ3727 emission mirrors the evolution of the declining volume of the H II region and thus closely matches the evolution and strength of Hβ emission except during the Wolf–Rayet phase, where [O II]λ3727 is further suppressed. These effects produce two classes of incidents of high O_{32} ratios: Case 1 (<1.5 Myr) where [O II]λ3727 doublet emission is strong and more likely to be detected, and Case 2 (3.7–5.2 Myr) where [O II]λ3727 doublet emission is relatively weak and therefore less likely to be detected. In the interval between the cases, O_{32} shortly falls to order unity before dipping further.

This toy model only calculates the contribution from a single instantaneous burst, but the broader simulation displays a tendency toward extended star formation events over tens of millions of years (see Figure 3, bottom plot showing specific star formation rates). Since several star particles are often formed in close spatial and temporal proximity in the simulation, each star formation event results in different emission line signatures due to the overlapping spectral phases of the contributing star particles during their evolution. The size and nature of their encompassing H II regions may also play a role, which in turn may depend on prior star formation
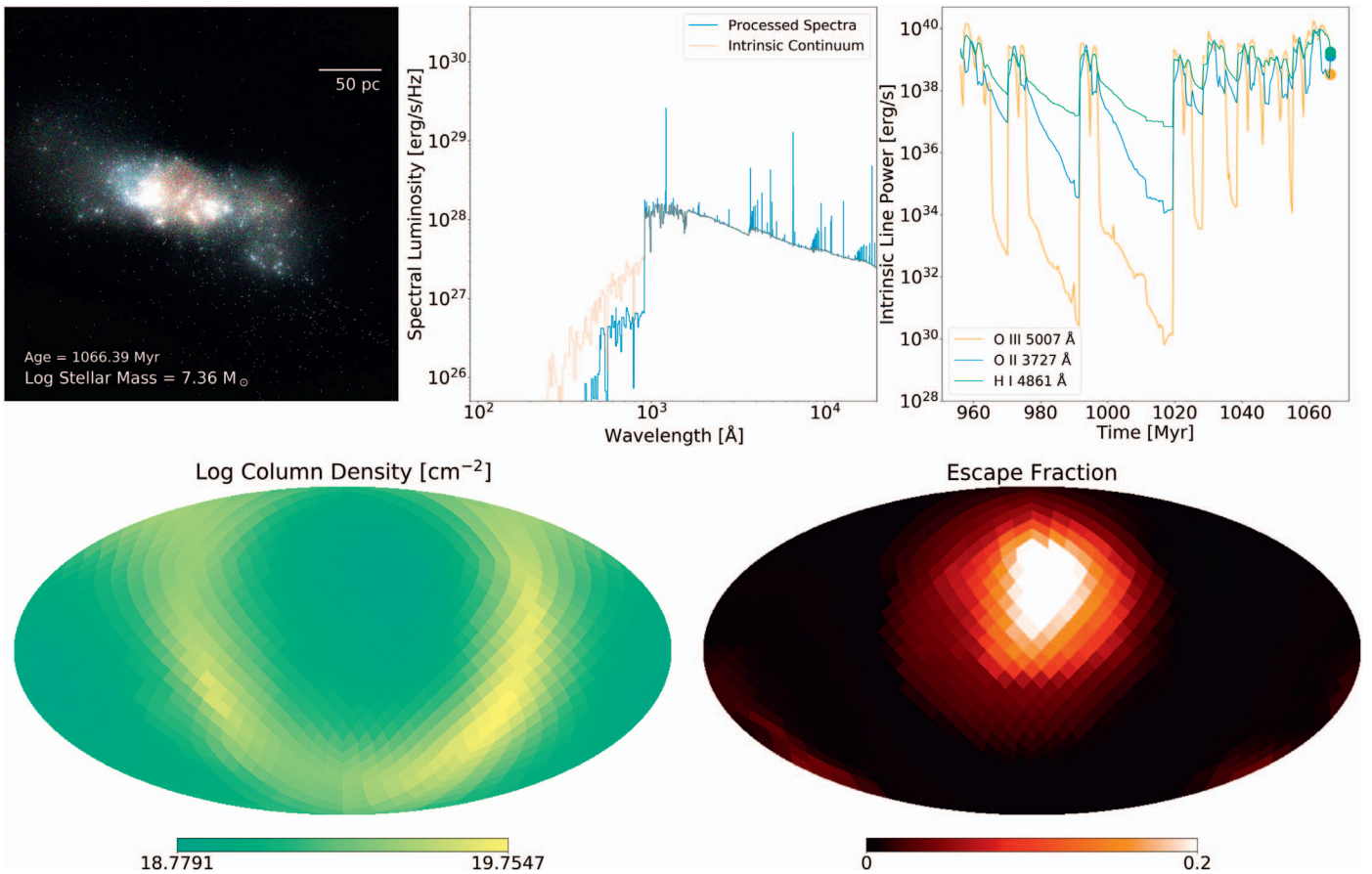
Figure 1. Key galactic characteristics of Halo 0's evolution, demonstrating the analysis pipeline. From stellar populations, visualized as light sources in the top left dust and gas Monte Carlo ray-tracing image, nebular emission lines are calculated throughout the halo to create a path-dependent processed spectra (seen in the middle top plot in a direction with high f_{esc}). Emission line strengths are tabulated every 368 ky to determine the time-series trend shown in the top right plot. To determine continuum absorption, radiation is absorbed through the medium using a wavelength-dependent absorption profile that mostly depends on the neutral hydrogen column density (shown in the bottom left as a function of path to the virial sphere). The resulting ionizing escape fraction (shown in the bottom right) is reported as a distribution of 972 ray-traced paths from each star and reported as a luminosity-weighted sum as further described in Section 2.3.
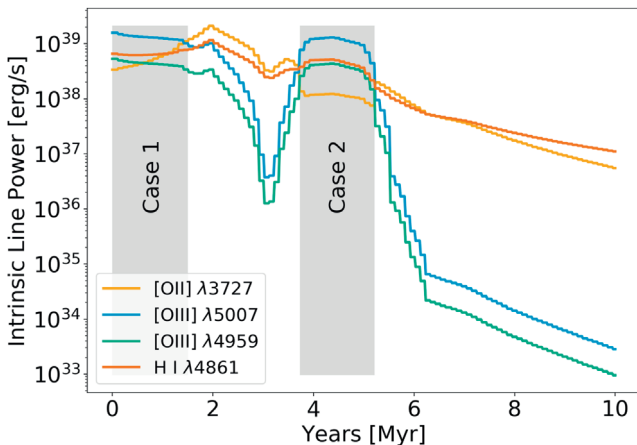

Figure 2. Toy CLOUDY converged emission line pattern resulting from a single, isolated $10^5 M_\odot$ starburst on a uniform sphere of gas with the same metallicity and density as Halo 0 at a simulation age of 1096 Myr. Emission line powers are shown for [O III], [O II], and Hβ as the star cluster spectra evolves using FSPS and the star cluster mass evolves using the mass age relationship described in Lamers et al. (2005). Regions where O_{32} is greater than 1 after the onset of star formation (Case 1) and during the Wolf–Rayet phase (Case 2) are shaded in gray.

episodes. Therefore, the exercise of classifying O_{32} peaks in a galactic context is most appropriate in the case of isolated bursty star formation events or isolated star-forming regions

and otherwise falls to degeneracies and stochastic peaks. It should also be noted that the existence of these cases is sensitive to the spectra assumptions of FSPS and the earliest few million years after a cluster forms is a challenging modeling problem (e.g., Senchyna et al. 2020).

3. Results

Armed with a generalized radiative transfer model for the production of emission lines within a high-resolution, cosmological simulation of an observably large galaxy, the trends in O_{32}, R_{23} escape fraction, and metallicity are described in the time domain to theoretically untangle observed correlations in high-redshift, high-escape fraction galaxies.

3.1. Time-dependent Trends

The topmost plot of Figure 3 displays the evolution of Halo 0 with respect to maximum f_{esc}, O_{32}, and R_{23} and provides context for the time dependence of the relevant phenomena. Each star formation incident is proceeded by an initial short-lived peak in O_{32} (Case 1), and followed by a subsequent stronger O_{32} peak (Case 2) as the spectra hardens during the Wolf–Rayet-powered phase of the star clusters. Bursts of star formation generate stellar and supernovae feedback that tempers subsequent star formation by photoionizing the ISM.
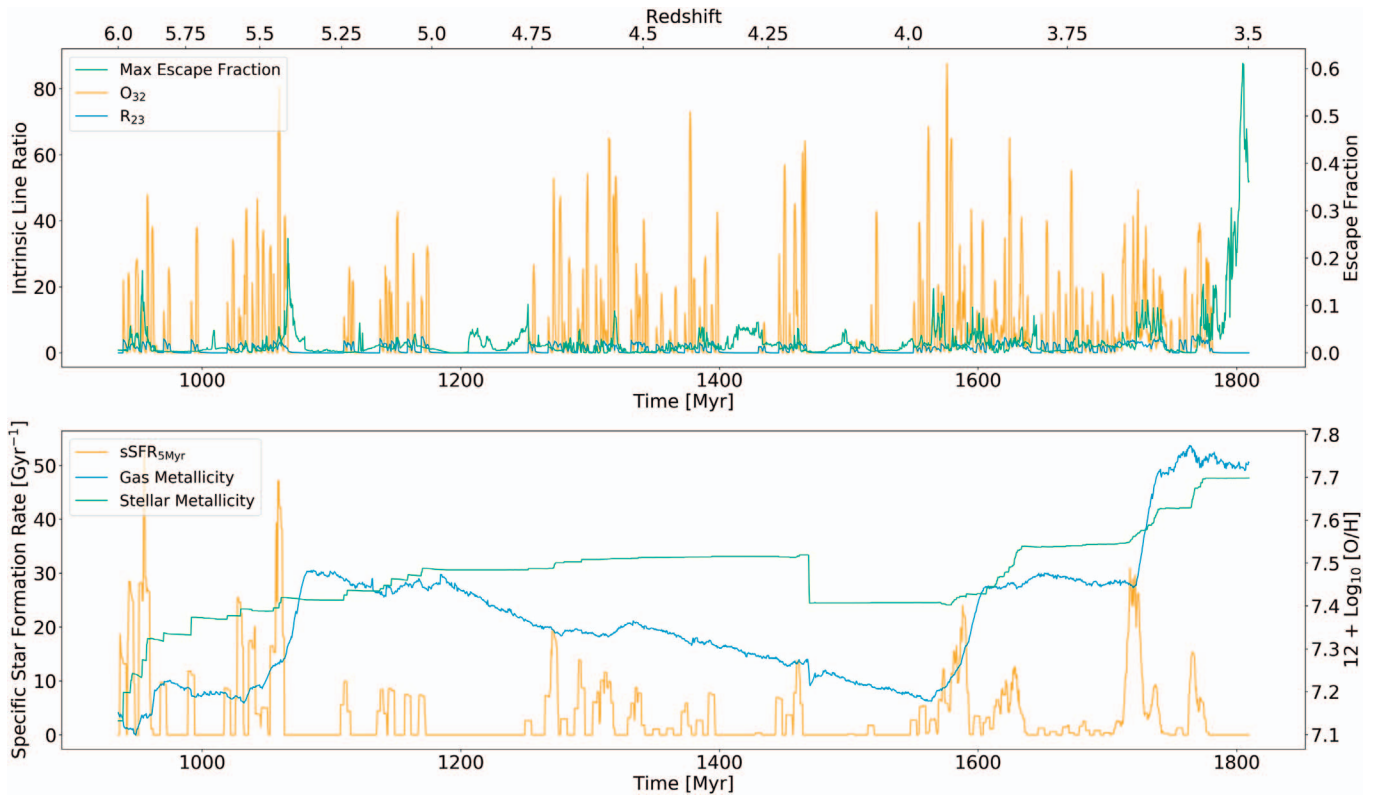
Figure 3. Time series plot of the observables and galactic characteristics of Halo 0 plotted at a 386 kyr cadence. Top plot: the maximum escape fraction among 972 galaxy orientations (green), O_{32} (salmon) and R_{23} (blue) ratios. Bottom plot: 5 Myr-averaged specific star formation rate (yellow, left y-axis), stellar metallicity (green), and gas metallicity (blue) plotted on the right y-axis.

Thus, high maximum f_{esc} values are rarely coincident with high O_{32} as the former are tied to minima of the star formation burst cycle. This pattern is repeated in Halo 1 and is not dissimilar from f_{esc} patterns in Ma et al. (2020).

As shown in the bottom plot of Figure 3, halo gas metallicity does not monotonically grow with stellar mass as low-metallicity gas inflows compete with enrichment from stellar feedback. The downward discontinuity in gas metallicity at $\sim$1470 Myr is an artifact of the redefinition of Halo 0 to include the merging, lower-metallicity Halo 1 and serves as a marker for the beginning of the merger process. During the merger, the galaxies make four relative periapsides with respect to each other before their bulges merge. Each periapsis drives a long, sustained episode of high star formation rates in both halos. This contrasts with the more sporadic bursts of star formation until the merger event and represents a distinctly dissimilar galactic environment to the pre-merger halos.

Gas mass fraction is physically connected to the escape fraction of ionizing radiation because it modulates the ionizing radiation density needed to create ionized channels through the halo. Low gas mass fractions are also correlated to low neutral hydrogen column densities (shown during the merger as a function of azimuthal and polar angle about the halo in the bottom left plot of Figure 1) and the peak and minimum column densities decrease by about one order of magnitude between $z = 6$ and $z = 3.5$. Halo 0's gas mass fraction within its virial radius declines from a high value of $f_{gas} = 0.29$ at the beginning of the window down to $f_{gas} = 0.16$ at the end of the window and then further declines to $f_{gas} = 0.10$ at $z = 3$. At $z = 3.5$, f_{esc} reaches its highest values, though highly anisotropically, as high star formation rates feed ionizing

radiation into a depleted reservoir of gas. In the 345 Myr interval between $z = 3.5$ and $z = 3.0$, no star formation occurs and the decrease of the gas mass fraction is explained by the gas-poor accumulation of dark matter into the halo from the remnants of the merger environment.

3.2. Relationship between f_{esc} and O_{32}

In Figure 3, there is a clear offset between the short period bursts of O_{32} and the longer period peaks of f_{esc}; however, a positive correlation between observed f_{esc} and O_{32} has been described in the literature. In this section, observations in the literature are detailed and then compared to synthetic observations calculated from the simulation to determine whether observed trends can be explained by time-dependent phenomena.

Figure 4 shows observationally inferred trends between f_{esc} and O_{32} (blue and red lines; Faisst 2016; Izotov et al. 2018). In addition to galaxies that fall within these trends, examples of galaxies with low f_{esc} and high O_{32} exist, such as J1011+1947, which has an $O_{32} \sim 36$ and $f_{esc} = 0.062$ or $f_{esc} = 0.114$ depending on the estimation method, or J1248+4259, which has an $O_{32} > 10$ and $f_{esc} \lesssim 0.03$ (Izotov et al. 2018). Recently, Bassett et al. (2019) added a single example (ID: 17251) of low O_{32} (0.37) and high f_{esc}(0.25) at $z \approx 3$ to the literature and challenged the notion that there is a trend between the two variables. These off-trend observations are indicated as red stars in Figure 4.

In the simulations of Halo 0 and Halo 1, observations of f_{esc} are both time-dependent and galaxy orientation-dependent as high f_{esc} values only escape into the IGM in highly focused channels (as shown in the bottom left plot of Figure 1),
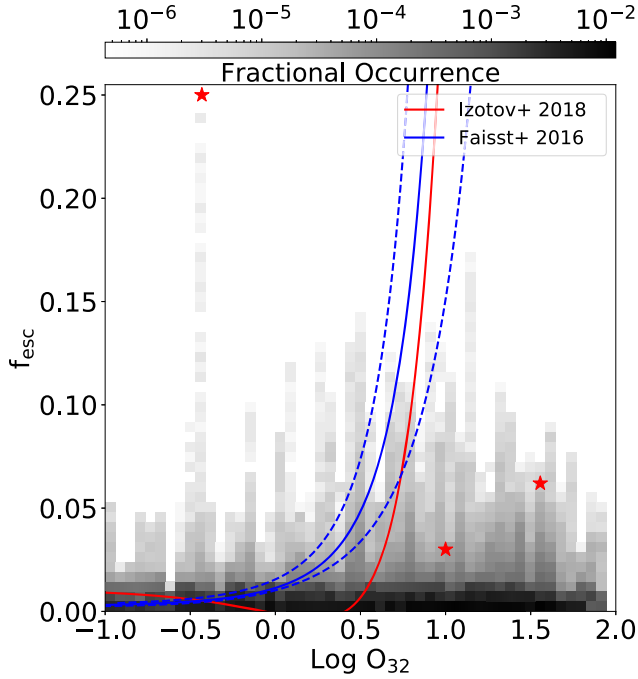
Figure 4. Plot of possible mock observations of $f_{\rm esc}$ vs. O_{32} during the evolution of Halo 0 plotted as a grayscale histogram. Also plotted are trend lines from Faisst (2016; blue with lower and upper bounds in dashed lines) and Izotov et al. (2018; red). Outlying observations noted in Section 3.2 are shown as red stars.

resulting in a distribution of possible observations at each time step. As described in Section 2.3, to compute this distribution, O_{32} values at each timestep are associated with 972 corresponding $f_{\rm esc}$ values in each of the HEALPIX directions, resulting in more than two million possible combinations for Halo 0 between $z = 6$ and $z = 3.5$. Combinations of mock observations of O_{32} and $f_{\rm esc}$ are then histogrammed by fractional occurrence and shown in grayscale in Figure 4.

3.2.1. Outlying Combinations of O_{32} and f_{esc}

The resulting simulated distribution roughly traces the distribution of observations including an outlying set of low O_{32} (<2) and high $f_{\rm esc}$ (>0.1) values similar to the outlying observation of 17251 from Bassett et al. (2019). Here we explore why this is rarely observed and falls outside the distribution of the rest of both the simulated and observed data.

Halo 0's examples of low O_{32} (0.34) and high $f_{\rm esc}$ ($\leqslant$0.24) occur at a single timestep of the 3400 studied ($t = 1066.39$ Myr, $M_\star = 10^{7.36}\,M_\odot$), which can be seen in the top plot of Figures 1, 3, and 4. This instance is about 5.5 Myr after the 5 Myr-averaged specific star formation rate of the halo reaches its highest value over the interval at $42.22\,{\rm Gyr}^{-1}$ ($30.51\,{\rm Gyr}^{-1}$ when averaged over 10 Myr), which corresponds to the end of the Case 2 phase of the O_{32} emission pattern. At time $t = 1066.39$ Myr, [O III] and [O II] emission line luminosities are falling rapidly and O_{32} is itself falling at a rate of about one order of magnitude every 368 kyr timestep. This decline follows several consecutive bursts of rapid star formation, when the distribution of gas in the galaxy is morphologically irregular (as seen in the true-color photon Monte Carlo image in the top left of Figure 1). Gaps in the gas open in the wake of strong supernovae feedback from prior star

formation events, and enable both an abnormally large H II region and a wide, ionized channel to the virial radius.

The highest escape fraction ($f_{\rm esc} = 0.077$) in Halo 1 registered when $O_{32} < 2$, but this occurs shortly before the first infall of the merger at $z = 4.27$ and may not be independent of the interaction with Halo 0. That incident is, however, also preceded by a $\sim$30 Myr period of sustained star formation with peaks in 5 Myr-averaged specific star formation rates in excess of $15\,{\rm Gyr}^{-1}$ that disrupt and precondition the gas for the formation of a larger H II region.

With sustained star formation, the minimum in O_{32} between the Case 1 and Case 2 phases is boosted by the constructive sum of stars in various phases of their evolution. Though most star formation events produce multiple star particles in our simulation, real clusters would likely have an even wider range of stellar ages that would further boost the O_{32} minima between Cases 1 and 2. Therefore, the drop in O_{32} at the end of the last Case 2 phase, which occurs at the end of a period of sustained star formation, presents the best opportunity for high $f_{\rm esc}$ with low O_{32} to be observed. However, that combination of conditions is several times rarer and more transient than other cases where O_{32} and/or $f_{\rm esc}$ can be observed. In the case of Halo 0, the combination of a large specific star formation rate after a long period of sustained star formation in an irregular and small galaxy suggests that the necessary conditions to produce low O_{32} and high $f_{\rm esc}$ were not impossibly rare.

From $z = 6$ until $z = 3$, less than 1 in 100,000 synthetic observations of Halo 0 or Halo 1 had a low (0.01–2) O_{32} and high (>0.1) $f_{\rm esc}$. However, more than 1 in 300 combinations of high (>0.1) $f_{\rm esc}$ and low to nonexistent (<0.01) O_{32} occurred. These fractions do not correspond to observational probabilities since they do not take into account telescope sensitivity limits and come from a limited sample of galaxies, but do elucidate trends that provide context to the current array of observations. Taken together, the top left region of Figure 4 (low O_{32} and high $f_{\rm esc}$) is almost completely depopulated for three reasons: (1) the phase offset between high $f_{\rm esc}$ and the presence of O_{32} due to feedback cycles, (2) the beaming of $f_{\rm esc}$ through ionized channels reducing the overall probability of high $f_{\rm esc}$ observations, and (3) the rarity of cases of low O_{32} due to it being a more transient state than nonexistent or high O_{32}. Conversely, in rare exceptions, outlier values in this region can be produced when conditions align. It should be noted that neither halo explores the full parameter space of observations or conditions as evidenced by the absence of incidences of higher $f_{\rm esc}$ like those reported in Nakajima et al. (2020) in Figure 4. A larger sample of simulated galaxies would be needed to make more general inferences about the observed rates.

Importantly, since O_{32} emission is optically thin and $f_{\rm esc}$ is anisotropic, there is *no direct causal connection* between O_{32} and $f_{\rm esc}$ in the simulations, despite the trend in observations. Each incident of O_{32} emission corresponds to a range of possible $f_{\rm esc}$ depending on the observer's orientation with respect to the galaxy and $f_{\rm esc}$ peaks occur on a longer timescale after star formation than an O_{32} peak.

3.3. Relationship between O_{32}, R_{23}, and Metallicity

Under the assumption of solar abundances, Halo 0 nonmonotonically traverses a $12 + {\rm Log}_{10}\,[{\rm O/H}]$ gas metallicity range from 7.10 to 7.77 over the stellar mass range of $6.92 < {\rm Log}\,[M_\star/M_\odot] < 8.31$ as it evolves from $z = 6$ to
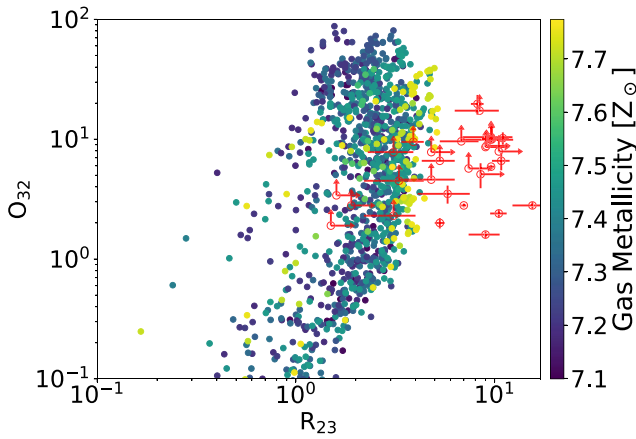
Figure 5. R_{23} vs. O_{32} trend of Halo 0 colored by metallicity (one point per timestep representing galaxy-wide line ratios) plotted with observations from Nakajima et al. (2020; red). Halo 0's line ratios cover a wide parameter space, but lie to the left of some of the observations due to the relationship between R_{23} and metallicity. Halo 1 (not shown) has an even lower-metallicity range ($6.94 \leqslant 12 + \mathrm{Log}_{10}\,[\mathrm{O/H}] \leqslant 7.24$) and its distribution is accordingly shifted to lower R_{23} by ~ 0.2 dex, while maintaining roughly the same overall shape.

$z = 3.5$. Compared to the sample of lower mass local galaxies from the Andrews & Martini (2013) SDSS metallicity-mass relationship, metallicities in this much higher redshift simulation scatter above and below the mean of the observed trend with a bias toward lower metallicities, especially at higher stellar masses.

The line ratio R_{23} is often used to estimate the metallicity of observed galaxies. Recently, data collected for high redshift ($z > 3$) high EW [O III] sources showed they occupy a range of $R_{23} \sim 1.5$–15.5 (Nakajima et al. 2020), as plotted with red error bars in Figure 5. Some of the lowest R_{23} ratios are lower bounds due to $H\beta$ and their true R_{23} may be larger. Similarly, the lower bounds in O_{32} plotted in Figure 5 could be significantly less than the true value owing to the presence of [O II]$\lambda 3727$ in the denominator.

To compare with the observations, synthetic R_{23} and O_{32} data from Halo 0 are shown in Figure 5, and colored by metallicity. The simulated galaxies at $z \sim 4$ have lower metallicities than many of the systems in the $z \sim 3$ Nakajima et al. (2020) sample, and both Halo 0 and Halo 1 (not shown) are offset to lower R_{23} given their lower metallicities. The distribution of O_{32} versus R_{23} values during the evolution of the simulated galaxies is more complicated, and properties beyond metallicity influence its behavior. While the highest O_{32} values in Halo 0 occurred at low metallicities and low R_{23}, Halo 1 displayed coincident peaks in O_{32} and R_{23} during its evolution. This difference suggests that where the maximum of O_{32} occurs relative to R_{23} is also connected to, e.g., a galaxy's specific star formation rate in addition to metallicity. For instance, during individual starbursts when there is a highly variable specific star formation rate, the O_{32} and R_{23} line ratios can rapidly move between low O_{32}-low R_{23} and high O_{32}-high R_{23} states, and can even show $R_{23} < 1$ for short intervals. However, scatter in O_{32} gradually decreases with increasing gas metallicity.

In summary, while our simulation reproduces many of the LACES observations of R_{23} and O_{32}, R_{23} analysis suggests that a higher gas metallicity simulated sample would be needed to cover the full range. Additionally, there is only weak evidence from our simulation that O_{32} and R_{23} or O_{32} and gas metallicity are clearly correlated in this metallicity regime and significant

time-dependent and metallicity-dependent scatter in those relationships exists due to other processes. However, as also seen in observations (e.g., Maiolino & Mannucci 2019), maximum values of O_{32} decrease with increasing metallicity and R_{23}. While that relationship might help guide comparisons between the work and higher metallicity observations, the scatter inherent in our synthetic line ratio calculations makes those comparisons challenging.

4. Discussion and Conclusions

Using high-resolution zoom-in simulations of star-forming galaxies at $z \sim 4$, a radiative transfer post-processing is used to explore the time evolution of the emission line ratios O_{32} and R_{23}, and the Lyman-continuum escape fraction f_{esc}. In summary, our key findings are as follows:

1. The simulations predict that high-escape fraction (e.g., $f_{\mathrm{esc}} > 0.05$) is almost always accompanied by high oxygen emission line ratios (e.g., $O_{32} > 3$). However, while f_{esc} and O_{32} are both powered by a hard ionizing spectra, the response time for the creation of an ionized channel that allows for high f_{esc} is much longer than the production of a high value of O_{32}, and thus the two phenomena are not causally related.
2. The combination of a low value of O_{32} and a high f_{esc} is likely a rare event that occurs at the end of a long burst of star formation and persists for only a few hundred thousand years.
3. Metallicity is degenerate on an O_{32} versus R_{23} plot due to tendency for the galaxy to move diagonally through the plane during star formation events.

Though this study was also able to explore more of the galaxy-scale dynamical nebular emission line parameter space than prior studies, our sample galaxies only occupy a portion of the observational space. A complementary recent study explored the statistics of these quantities in static outputs of multigalaxy simulations (Katz et al. 2020), and the results are broadly consistent despite this study's focus on examining the time-evolution of only a pair galaxies. Given the importance of the relative time evolution of f_{esc} and O_{32}, a larger sample of simulated galaxies with sufficient time cadence to make statistical arguments about the nature and evolution of nebular emission lines is still required and will be explored in future work.

ORCID iDs

Kirk S. S. Barrow ⓘ https://orcid.org/0000-0002-8638-1697
Brant E. Robertson ⓘ https://orcid.org/0000-0002-4271-0364
Richard S. Ellis ⓘ https://orcid.org/0000-0001-7782-7071
Kimihiko Nakajima ⓘ https://orcid.org/0000-0003-2965-5070

Aayush Saxena ⬤ https://orcid.org/0000-0001-5333-9970

References

Andrews, B. H., & Martini, P. 2013, ApJ, 765, 140
Bañados, E., Venemans, B. P., Mazzucchelli, C., et al. 2018, Natur, 553, 473
Barrow, K. S. S. 2019, MNRAS, 491, 4509
Bassett, R., Ryan-Weber, E. V., Cooke, J., et al. 2019, MNRAS, 483, 5223
Borthakur, S., Heckman, T. M., Leitherer, C., & Overzier, R. A. 2014, Sci, 346, 216
Bouwens, R. J., Illingworth, G. D., Oesch, P. A., et al. 2015, ApJ, 811, 140
Bryan, G. L., Norman, M. L., O'Shea, B. W., et al. 2014, ApJS, 211, 19
Conroy, C., & Gunn, J. E. 2010, ApJ, 712, 833
Draine, B. T. 2003, ARA&A, 41, 241
Draine, B. T. 2011, Physics of the Interstellar and Intergalactic Medium (Princeton, NJ: Princeton Univ. Press)
Du, X., Shapley, A. E., Tang, M., et al. 2020, ApJ, 890, 65
Faisst, A. L. 2016, ApJ, 829, 99
Fan, X., Narayanan, V. K., Lupton, R. H., et al. 2001, AJ, 122, 2833
Fan, X., Strauss, M. A., Becker, R. H., et al. 2006, AJ, 132, 117
Ferland, G. J., Chatzikos, M., Guzmán, F., et al. 2017, RMxAA, 53, 385
Finkelstein, S. L., D'Aloisio, A., Paardekooper, J.-P., et al. 2019, ApJ, 879, 36
Fletcher, T. J., Tang, M., Robertson, B. E., et al. 2019, ApJ, 878, 87
Geen, S., Hennebelle, P., Tremblin, P., & Rosdahl, J. 2015, MNRAS, 454, 4484
Górski, K. M., Hivon, E., Banday, A. J., et al. 2005, ApJ, 622, 759
Grazian, A., Giallongo, E., Gerbasi, R., et al. 2016, A&A, 585, A48
Gunn, J. E., & Peterson, B. A. 1965, ApJ, 142, 1633
Inoue, A. K., Shimizu, I., Iwata, I., & Tanaka, M. 2014, MNRAS, 442, 1805
Iwata, I., Inoue, A. K., Matsuda, Y., et al. 2009, ApJ, 692, 1287
Izotov, Y. I., Orlitová, I., Schaerer, D., et al. 2016a, Natur, 529, 178
Izotov, Y. I., Schaerer, D., Thuan, T. X., et al. 2016b, MNRAS, 461, 3683
Izotov, Y. I., Schaerer, D., Worseck, G., et al. 2020, MNRAS, 491, 468
Izotov, Y. I., Worseck, G., Schaerer, D., et al. 2018, MNRAS, 478, 4851
Jaskot, A. E., Dowd, T., Oey, M. S., Scarlata, C., & McKinney, J. 2019, ApJ, 885, 96
Jaskot, A. E., & Oey, M. S. 2013, ApJ, 766, 91
Kahre, L., Walterbos, R. A., Kim, H., et al. 2018, ApJ, 855, 133
Katz, H., Ďurovčíková, D., Kimm, T., et al. 2020, MNRAS, 498, 164
Kim, J.-h., Abel, T., Agertz, O., et al. 2014, ApJS, 210, 14

Lamers, H. J. G. L. M., Gieles, M., Bastian, N., et al. 2005, A&A, 441, 117
Leitherer, C., Hernandez, S., Lee, J. C., & Oey, M. S. 2016, ApJ, 823, 64
Ma, X., Hopkins, P. F., Kasen, D., et al. 2016, MNRAS, 459, 3614
Ma, X., Quataert, E., Wetzel, A., et al. 2020, MNRAS, 498, 2001
Madau, P. 1995, ApJ, 441, 18
Maiolino, R., & Mannucci, F. 2019, A&ARv, 27, 3
Meštrić, U., Ryan-Weber, E. V., Cooke, J., et al. 2020, MNRAS, 494, 4986
Mostardi, R. E., Shapley, A. E., Nestor, D. B., et al. 2013, ApJ, 779, 65
Mostardi, R. E., Shapley, A. E., Steidel, C. C., et al. 2015, ApJ, 810, 107
Naidu, R. P., Forrest, B., Oesch, P. A., Tran, K.-V. H., & Holden, B. P. 2018, MNRAS, 478, 791
Nakajima, K., Ellis, R. S., Iwata, I., et al. 2016, ApJL, 831, L9
Nakajima, K., Ellis, R. S., Robertson, B. E., Tang, M., & Stark, D. P. 2020, ApJ, 889, 161
Nakajima, K., Fletcher, T., Ellis, R. S., Robertson, B. E., & Iwata, I. 2018, MNRAS, 477, 2098
Nakajima, K., & Ouchi, M. 2014, MNRAS, 442, 900
Nestor, D. B., Shapley, A. E., Kornei, K. A., Steidel, C. C., & Siana, B. 2013, ApJ, 765, 47
Nestor, D. B., Shapley, A. E., Steidel, C. C., & Siana, B. 2011, ApJ, 736, 18
Planck Collaboration, Aghanim, N., Akrami, Y., et al. 2020, A&A, 641, A6
Rémy-Ruyer, A., Madden, S. C., Galliano, F., et al. 2014, A&A, 563, A31
Robertson, B. E., Ellis, R. S., Furlanetto, S. R., & Dunlop, J. S. 2015, ApJL, 802, L19
Senchyna, P., Stark, D. P., Charlot, S., et al. 2020, arXiv:2008.09780
Shapley, A. E., Steidel, C. C., Pettini, M., Adelberger, K. L., & Erb, D. K. 2006, ApJ, 651, 688
Smith, B. M., Windhorst, R. A., Cohen, S. H., et al. 2020, ApJ, 897, 41
Smith, B. M., Windhorst, R. A., Jansen, R. A., et al. 2018, ApJ, 853, 191
Steidel, C. C., Bogosavljević, M., Shapley, A. E., et al. 2018, ApJ, 869, 123
Steidel, C. C., Pettini, M., & Adelberger, K. L. 2001, ApJ, 546, 665
Tang, M., Stark, D. P., Chevallard, J., & Charlot, S. 2019, MNRAS, 489, 2572
Trebitsch, M., Blaizot, J., Rosdahl, J., Devriendt, J., & Slyz, A. 2017, MNRAS, 470, 224
Vanzella, E., Giavalisco, M., Inoue, A. K., et al. 2010, ApJ, 725, 1011
Vanzella, E., Guo, Y., Giavalisco, M., et al. 2012, ApJ, 751, 70
Wise, J. H., Abel, T., Turk, M. J., Norman, M. L., & Smith, B. D. 2012, MNRAS, 427, 311
Yamanaka, S., Inoue, A. K., Yamada, T., et al. 2020, MNRAS, 498, 3095